Remote Sensing of Environment 134 (2013) 39–49

Contents lists available at SciVerse ScienceDirect

Remote Sensing of Environment

journal homepage: www.elsevier.com/locate/rse

Investigating assumptions of crown archetypes for modelling LiDAR returns

Kim Calders [a,*], Philip Lewis [b], Mathias Disney [b], Jan Verbesselt [a], Martin Herold [a]

[a] Laboratory of Geo-Information Science and Remote Sensing, Wageningen University, Droevendaalsesteeg 3, Wageningen 6708 PB, The Netherlands
[b] Department of Geography, University College London, Gower Street, London WC1E 6BT, UK

ARTICLE INFO

Article history:
Received 25 December 2011
Received in revised form 11 February 2013
Accepted 14 February 2013
Available online xxxx

Keywords:
LiDAR
Waveform
Radiative transfer
Crown archetype
LAI
Inversion

ABSTRACT

LiDAR has the potential to derive canopy structural information such as tree height and leaf area index (LAI), via models of the LiDAR signal. Such models often make assumptions regarding crown shape to simplify parameter retrieval and crown archetypes are typically assumed to contain a turbid medium to account for within-crown scattering. However, these assumptions may make it difficult to relate derived structural parameters to measurable canopy properties. Here, we test the impact of crown archetype assumptions by developing a new set of analytical expressions for modelling LiDAR signals. The expressions for three crown archetypes (cuboids, cones and spheroids) are derived from the radiative transfer solution for single order scattering in the optical case and are a function of crown macro-structure (height and crown extent) and LAI. We test these expressions against waveforms simulated using a highly-detailed 3D radiative transfer model, for LAI ranging from one to six. This allows us to control all aspects of the crown structure and LiDAR characteristics. The analytical expressions are fitted to both the original and the cumulative simulated LiDAR waveforms and the CV(RMSE) of model fit over archetype trees ranges from 0.3% to 21.2%. The absolute prediction error (APE) for LAI is 7.1% for cuboid archetypes, 18.6% for conical archetypes and 4.5% for spheroid archetypes. We then test the analytical expressions against more realistic 3D representations of broadleaved deciduous (birch) and evergreen needle-leaved (Sitka spruce) tree crowns. The analytical expressions perform more poorly (APE values up to 260.9%, typically ranging from 39.4% to 78.6%) than for the archetype shapes and ignoring clumping and lower branches has a significant influence on the performance of waveform inversion of realistic trees. The poor performance is important as it suggests that the assumption of crown archetypes can result in significant errors in retrieved crown parameters due to these assumptions not being met in real trees. Seemingly reasonable inferred values may arise due to coupling between parameters. Our results suggest care is needed in inferring biophysical properties based on crown archetypes. Relationships between the derived parameters and their physical counterparts need further elucidation.

1. Introduction

Forest structure plays an important role in forest ecosystems. Leaf area index (LAI) is a meaningful structural parameter, since several biological and physical processes are related to the total leaf surface. For example, photosynthesis, respiration, transpiration, carbon and nutrient cycles, and rainfall interception are functions of forest structure and LAI.

Active sensors such as LiDAR (light detection and ranging) can measure something approximating retroreflectance as a time or distance resolved signal over forest canopies. LiDAR therefore can serve as an excellent tool to assess forest structure and the three-dimensional distribution of plant canopies (Koch et al., 2006; Lefsky et al., 1999; Nelson, 1997; Vauhkonen et al., 2009). Although many studies have examined the possibilities that LiDAR offers in structure assessment, little work has been conducted on quantitative LiDAR data interpretation, i.e. relating the LiDAR signal to the fundamental principles governing the scattered signal. Barbier et al. (2011) studied how canopy structure interacts with physical signals (light) at forest stand level. However, a better understanding of the physical underpinnings of light interaction with canopy structure at tree level is needed, for example, to optimise fusion with optical and LiDAR data. In this study, we will therefore look at single tree LiDAR signals in an effort to understand the information content of such LiDAR signals. Here, the relationship between LiDAR and vegetation structure is studied and quantified in the nadir direction.

Many LiDAR studies are based on the assumptions of crown archetypes and some examples are listed in Table 1. Ferraz et al. (2012), Riaño et al. (2004), Lim et al. (2003) and Ni-Meister et al. (2001) assumed ellipsoidal crowns. North et al. (2010) and Wang and Glenn (2008) used both conical and ellipsoidal crown shapes to characterise the crown. Goodwin et al. (2007) described crowns as hemi-ellipsoids and Koetz et al. (2007) also assumed crowns were shaped as hemi-ellipsoids when simulating large footprint LiDAR over simulated forest stands. Hyde et al. (2005) used four archetypes to characterise the trees in their study area: elliptical, umbrella-shaped, conical and cylindrical. They used vegetation type as a proxy for crown shape, e.g. stands of

* Corresponding author. Tel.: +31 317 485257; fax: +31 317 419000.
E-mail address: kim.calders@wur.nl (K. Calders).

0034-4257/$ – see front matter © 2013 Elsevier Inc. All rights reserved.
http://dx.doi.org/10.1016/j.rse.2013.02.018

Table 1
Examples of LiDAR studies using crown archetypes.

Reference	Crown archetype
Ferraz et al. (2012)	Ellipsoidal
North et al. (2010)	Ellipsoidal & Conical
Wang and Glenn (2008)	Ellipsoidal & Conical
Koetz et al. (2007)	Hemi-ellipsoidal
Goodwin et al. (2007)	Hemi-ellipsoidal
Hyde et al. (2005)	Elliptical, Umbrella-shaped, Conical & Cylindrical
Riaño et al. (2004)	Ellipsoidal
Lim et al. (2003)	Ellipsoidal
Ni-Meister et al. (2001)	Ellipsoidal
Sun and Ranson (2000)	Ellipsoidal, Conical & Hemi-ellipsoidal

pure red fir were assumed to be conical or pointed, while deciduous crowns were assumed to be more rounded. Sun and Ranson (2000) modelled crown shapes as cones, ellipsoids and hemi-ellipsoids. Kato et al. (2009) did not make assumptions about some sort of archetype but used a wrapped surface reconstruction approach based on the LiDAR point cloud to generate the crown shape. A common approach to describe the distribution of foliage within archetype crowns is to use a turbid medium model, which assumes a constant leaf area density throughout the crown (Koetz et al., 2007; North et al., 2010; Sun & Ranson, 2000).

Earlier work on complex modelling approaches for LiDAR waveforms mainly focused on understanding some of the influences on the waveform. Sun and Ranson (2000) presented a 3D model for simulating LiDAR waveforms from forest stands. Their results showed that LiDAR waveforms are an indication of both horizontal and vertical structures of forest canopies. Kotchenova et al. (2003) introduced a time-dependent stochastic radiative transfer theory, which allowed for a more realistic description of clumping and gaps. Ni-Meister et al. (2001) used a hybrid geometric optical and radiative transfer model (GORT) to interpret the LiDAR waveforms with respect to canopy structure and validated their findings using SLICER data. Gap probability was identified as the most important link between canopy structure and modelling LiDAR waveforms. LiDAR simulations in Blair and Hofton (1999) suggested that multiple scattering in vegetation canopies did not contribute significantly to the LiDAR waveform shape and several other LiDAR modelling studies also assumed single scattering only (Goodwin et al., 2007; Ni-Meister et al., 2001; Sun & Ranson, 2000).

Empirical relationships often make assumptions, which lead us away from the fundamental scattering properties, making it hard to relate the derived structural parameters to real canopies. In this study we return to a limited number of assumptions based on radiative transfer (RT). These assumptions are: crown archetypes, constant leaf area density throughout the crown and first order scattering. We adopt these widely-used assumptions in order to quantify their impact in deriving canopy parameters from LiDAR observations. We address the question of whether simple crown archetype assumptions can be used to model LiDAR scattering. If these assumptions hold up, analytical expressions for LiDAR scattering would be preferred over empirical relationships, because those analytical solutions will allow retrieval of crown parameters that are physically interpretable. If such crown archetype assumptions are shown not to be valid, the analytical expressions will give insight into why this is and what implications this will have for inverting LiDAR signals using these assumptions. The main objectives of this paper are:

1. The derivation of analytical formulae that express LiDAR reflectivity as a function of crown macro-structure parameters and crown leaf area density for a nadir configuration;
2. The testing of these formulae against realistic LiDAR simulations; and
3. The quantification of impact of crown archetype assumptions on retrieval of LAI.

Such formulae, for single trees, are potentially of great value themselves for understanding and deriving information. Solving for canopy properties using analytical expressions allows crown structure to be extracted from LiDAR waveforms. We present analytical expressions for a nadir configuration obtained by solving the 3D integral for photon transport in a specific envelope crown shape. We test these expressions by comparison with realistic LiDAR simulations of which all variables are known. Various 3D tree models are created, which conform to the assumptions underlying our analytical expressions. LiDAR signals from these crowns are simulated using a Monte Carlo ray tracing radiative transfer model. In this way, we can control all aspects of the crown structure and the (simulated) signal properties, which would not be possible using measured LiDAR data. Trees with simple archetype crown shapes are analysed first to fully understand these waveforms. More realistic representations of broadleaved deciduous (birch) and evergreen needle-leaved (Sitka spruce) trees are then considered, which we use to elucidate some of the more interesting aspects of when and why simple models might fail. Finally, we discuss the likely impact of assumptions of crown archetypes on interpreting LiDAR signals and we outline ways in which these impacts can be quantified. This work is of importance due to the increasing requirement for accurate, physically-realistic retrieval of canopy parameters from LiDAR data.

2. Methods

2.1. Describing LiDAR reflectivity as a function of tree structure

In this section, we derive analytical formulae to describe LiDAR reflectivity as a function of different structural tree parameters for a nadir configuration. We use an approach based on the solution to the scalar radiative transfer equation for a plane parallel medium, which assumes vertical homogeneity within canopy layers and Lambertian scattering from objects. We then adjust the solution for the standard case for vertical heterogeneity inside the canopy. As a result, we can describe light passing through archetype crown shapes as cuboids, cones and prolate spheroids (hereafter referred to as spheroids). Several LiDAR studies (Goodwin et al., 2007; Ni-Meister et al., 2001; Sun & Ranson, 2000) assumed single scattering only and LiDAR simulations over vegetation canopies in Blair and Hofton (1999) suggested that there was no significant contribution of multiple scattering to the LiDAR waveform shape. We tested that for a spheroid archetype more than 98.5% of the returned LiDAR reflectance was coming from the first order scattering when there was a single tree in the LiDAR footprint. Testing over a canopy with multiple trees in the LiDAR footprint showed a first order scattering domination of 91.1%. All tests were done at wavelength of 1064 nm for plate leaf crowns using the *librat* radiative transfer model with settings specified in Section 2.2.2. It is therefore a reasonable assumption to only consider first order scattering (i.e. only one interaction with soil or canopy elements) in this study.

2.1.1. A solution to the scalar radiative transfer equation for a LiDAR signal

The solution for first order scattering in the optical case is used to reconstruct the LiDAR waveform over a plane parallel canopy medium theoretically (see Fig. 1). If Ω_s is the direction of scattering and Ω_0 the direction of the incident LiDAR pulse then $I(\Omega_s, z)$ is the received single scattering energy by the sensor at depth z in direction Ω_s over a plane parallel canopy.

$$I(\Omega_s,z) = e^{\frac{-\kappa_e(\Omega_s)(z-(-H))}{\mu_s}} \rho_{soil}(\Omega_s,\Omega_0) e^{\frac{-\kappa_e(\Omega_0)(-H)}{\mu_0}} I_0 d(\Omega_s-\Omega_0) + \frac{I_0}{\mu_s}\int_{Z=-H}^{Z=z} e^{\frac{-\kappa_e(\Omega_s)(z-Z)}{\mu_s}} e^{\frac{\kappa_e(\Omega_0)Z}{\mu_0}} P(\Omega_0\rightarrow\Omega_s)dZ \quad (1)$$

I_0 refers to the incident radiation intensity on top of the canopy. The volume scattering phase function is defined as $P(\Omega_0\rightarrow\Omega_s) =$

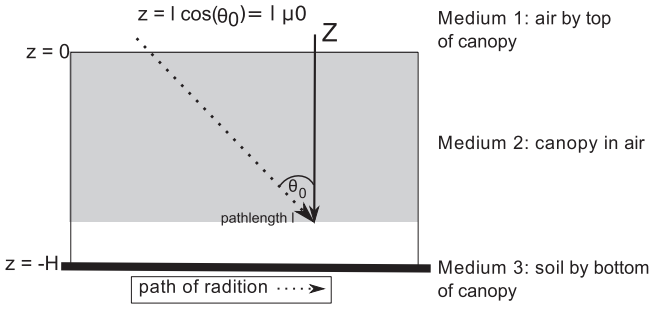

Fig. 1. Overview of a plane parallel canopy medium: the top of the canopy is at $z = 0$ and the path of radiation has length l.

$\frac{u_l}{\mu_s}\Gamma(\Omega_0 \rightarrow \Omega_s)$ where $\Gamma(\Omega_0 \rightarrow \Omega_s)$ is the area scattering phase function. The volume scattering phase function defines that part of the radiation coming in the direction Ω_0 which is scattered by a unit volume in a particular direction Ω_s. The area scattering phase function is the part of the radiation coming in the direction Ω_0 which is scattered by a unit area in a particular direction Ω_s (Ross, 1981). u_l is the leaf area density function, which describes the area of leaves per unit volume. μ is the cosine of the direction vector Ω with the local normal, Z, and accounts for path length through the canopy. In this study, the sensor emits and receives LiDAR pulses at nadir and therefore μ_s and μ_0 were equal to $\cos(0°) = 1$. Both μ_s and μ_0 need to be re-introduced to work out the equations for off-nadir conditions. In the specific case of a LiDAR sensor, $\Omega_s = -\Omega_0$ and therefore this direction is called Ω. The optical extinction coefficient κ_e describes the probability per unit length that a photon encounters a canopy element in the direction of travel. According to Ross (1981), κ_e can be written as $u_l G(\Omega)$. $G(\Omega)$ is the foliage orientation function and equals the projection of a unit area of foliage on a plane perpendicular to the direction Ω, averaged over elements of all orientations. LiDAR sensors operate in the so-called hotspot, i.e. where view and illumination angles coincide. In this retroreflection direction the probability of a photon being able to follow the same path back up through the canopy as it took on its way down through the canopy is 1 and therefore we need to account for the joint gap probability. We are not only interested in the final returned energy, but also in the intermediate interactions at each level of z. Therefore Eq. (1) can be integrated with different limits of $[0,-z]$, where z is any value between 0 (i.e. top of the canopy: see Fig. 1) and H (i.e. tree height). The received single scattering energy by the LiDAR sensor, looking in a specific direction Ω, as function of canopy depth z can be expressed as $I(\Omega,0,z)$. The 0 in $I(\Omega,0,z)$ indicates that the LiDAR sensor is located above the canopy ($z = 0$ at the top of the canopy);

$$I(\Omega,0,z) = e^{-G(\Omega)u_l H}\rho_{soil}(\Omega)I_0 d(\Omega) + \frac{I_0\Gamma(\Omega\rightarrow-\Omega)}{G(\Omega)}\left[1-e^{-G(\Omega)u_l z}\right] \quad (2)$$

The focus of this study is on describing the LiDAR waveform of the crown, which is a plane parallel canopy in this section. For ease of reference, only the crown contribution of Eq. (2) will therefore be considered in the derivation of the analytical expressions, i.e.

$$I(\Omega,0,z)_{crown} = \frac{I_0\Gamma(\Omega\rightarrow-\Omega)}{G(\Omega)}\left[1-e^{-G(\Omega)u_l z}\right] \quad (3)$$

To reconstruct the LiDAR waveform, the contribution of each individual infinitesimal horizontal crown layer is needed. This is achieved by taking the derivative with respect to z:

$$\frac{dI(\Omega,0,z)_{crown}}{dz} = I_0\Gamma(\Omega\rightarrow-\Omega)u_l e^{-G(\Omega)u_l z} \quad (4)$$

2.1.2. Interpretation of LiDAR waveforms over single crown archetypes

In this section we derive analytical expressions to describe LiDAR waveforms over single crown archetypes for a nadir configuration. An analytical description of the waveform is preferred over a numerical approach, because it establishes a direct and stronger link with effective crown structure parameters. In Section 2.1.1 we described the analytical expression for a LiDAR waveform of a plane parallel canopy medium, which implied that the whole of the LiDAR footprint is covered by the canopy. This is not necessarily true when we use single trees and therefore we will introduce a factor C that accounts for the portion of the LiDAR footprint that is covered by the horizontal crown extent. C is therefore the canopy cover, which can range from zero to one.

Our approach treats the crown shapes as a summation of homogeneous annuli with equal effective penetration depth z' centred around the vertical axis (i.e. elevation axis). Unlike a numerical approach, the vertical interval (i.e. the bin step) and annulus width are infinitesimal and therefore the analytical expression can be seen as an integral.

By definition, the effective penetration depth (z') within the plane parallel canopy medium is constant throughout the extent of any horizontal layer. The top of the canopy was earlier defined as the origin of the z-axis ($z = 0$) and therefore the value z (the depth with respect to the top of the canopy) is equal to the value z' (the effective penetration depth within the crown) for a plane parallel canopy. This is also true for cuboid crown archetypes since the horizontal extent of each horizontal crown layer is constant. This is not the case for irregular crown shapes (conical and spheroid). For these crown archetypes the horizontal extent changes with depth into the crown, which is illustrated in Figs. 2 and 3 and discussed below.

2.1.2.1. Cuboid archetypes. The top of the crown in this case is a horizontal plane and z' is constant throughout the extent of any horizontal layer (i.e. z equals z' at any position in a horizontal layer). Therefore we can describe the behaviour of photons passing through a cuboid crown by introducing the canopy cover C to Eq. (4):

$$\frac{dI(\Omega,0,z)_{crown}}{dz} = CI_0\Gamma(\Omega\rightarrow-\Omega)u_l e^{-G(\Omega)u_l z} \quad (5)$$

This expression can be solved for LAI by substituting $\frac{A_{cover}LAI}{V_{tot}}$ for u_l where A_{cover} is the area of the tree cover projection and V_{tot} the total

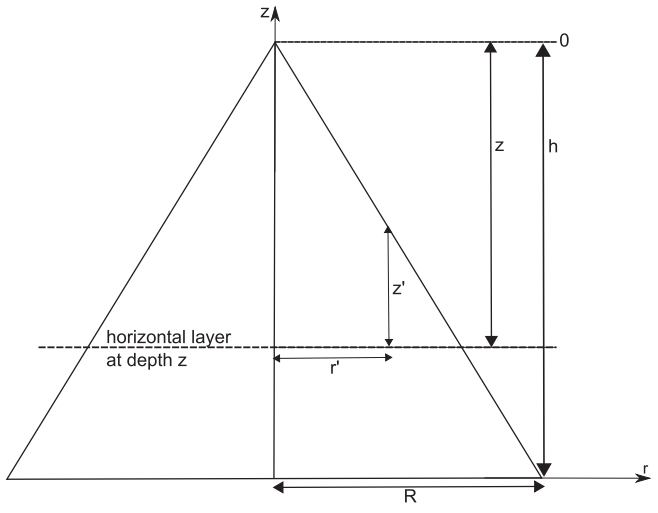

Fig. 2. The vertical cross section of conical crown. z is the depth with respect to the top of the canopy and z' is the effective penetration depth within the crown. R is the maximum crown radius at $z = h$. For a horizontal layer at depth z, the radius at this depth, r, equals $\frac{Rz}{h}$. At this layer, r' can be any intermediate position in the interval $\left[0,\frac{Rz}{h}\right]$.

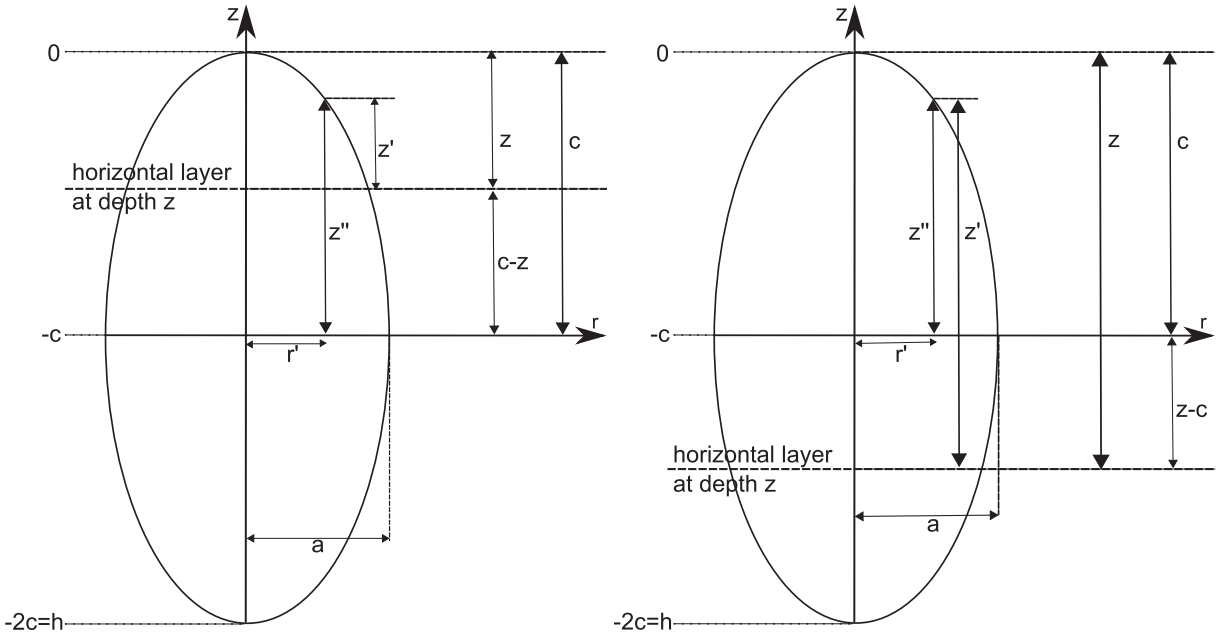

Fig. 3. The vertical cross section of a spheroid crown is an ellipse described by $1 = \frac{r'^2}{a^2} + \frac{z'^2}{c^2}$ where a is the semi-minor radius and c is the semi-major radius. z is the depth with respect to the top of the canopy and z' is the effective penetration depth within the crown. For a horizontal layer at depth z, the radius at this depth is r and r' can be any intermediate position in the interval [0,r]. (left) Upper hemisphere; (right) Lower hemisphere.

tree volume. For cuboid archetypes this substitution therefore becomes $u_l = \frac{LAI}{h}$ where h is the crown height.

2.1.2.2. Conical archetypes. In this case, within one horizontal layer at a specific depth z, different parts of the crown will be subject to different within-crown path length z'. Therefore the expression for the general (cuboid) case needs to be adjusted for shapes which have different z' values within a single horizontal layer. Based on Eq. (5), it follows that

$$\frac{dI(\Omega,0,z)_{crown}}{dz} = CI_0\Gamma(\Omega\rightarrow-\Omega)u_l e^{-G(\Omega)u_l z'} \tag{6}$$

Each horizontal layer can be seen as the sum of infinitesimal annuli with constant z'. The reflectance of each annulus is the product of Eq. (6) with its area. The total reflectance of a horizontal layer therefore is the integral over all the annuli. Fig. 2 illustrates that for a horizontal layer at depth z, the radius at this depth, r, equals $\frac{Rz}{h}$. R is the maximum crown radius at $z = h$. Therefore the integral needs to be calculated for the r' interval $\left[0, \frac{Rz}{h}\right]$, where r' can be any intermediate position in the interval. Normalising is achieved by dividing by πR^2:

$$\frac{dI(\Omega,0,z)_{crown}}{dz} = C\int_{r'=0}^{r'=\frac{Rz}{h}} \frac{I_0\Gamma(\Omega\rightarrow-\Omega)u_l\left(e^{-G(\Omega)u_l z'}\right)2\pi r'\,dr'}{\pi R^2} \tag{7}$$

From Fig. 2 it can be seen that z' is a function of z and r' : $z' = z - \frac{hr'}{R}$ and the integral (Eq. 7) can be solved, giving

$$\frac{dI(\Omega,0,z)_{crown}}{dz} = C\frac{2I_0\Gamma(\Omega\rightarrow-\Omega)}{h^2G(\Omega)}\left(z - \frac{1}{G(\Omega)u_l} + \frac{e^{-G(\Omega)u_l z}}{G(\Omega)u_l}\right) \tag{8}$$

This expression can also be expressed as a function of LAI by substituting $\frac{3LAI}{h}$ for u_l.

2.1.2.3. Spheroid archetypes. Based on Fig. 3, the equation of the ellipse (i.e. the vertical cross section of the prolate spheroid) can be written as $1 = \frac{r'^2}{a^2} + \frac{z''^2}{c^2}$ and therefore $z'' = c\sqrt{1-\frac{r'^2}{a^2}}$ and $r' = a\sqrt{1-\frac{z''^2}{c^2}}$ where (r', z'') are the locations of the points on the surface of the envelope that shape the ellipse. r' is rewritten in terms of z as $a\sqrt{1-\frac{(c-z)^2}{c^2}}$ and will serve as the upper boundary of the integral over r'. For the upper hemisphere of the crown, z' can be expressed as $z''-(c-z) = c\sqrt{1-\frac{r'^2}{a^2}}-(c-z)$. The expression for the spheroid case is obtained similar to Eq. (7) since spheroids and cones both have circular horizontal cross sections (for the spheroid case $R = a$).

$$\frac{dI(\Omega,0,z)_{crown,\ upper}}{dz} = C\frac{2I_0\Gamma(\Omega\rightarrow-\Omega)}{G(\Omega)c}\left(\frac{c-z}{c} + \frac{1}{G(\Omega)u_l c} - e^{-G(\Omega)u_l z}\left(1 + \frac{1}{G(\Omega)u_l c}\right)\right) \tag{9}$$

In Fig. 3 it can be seen that the expression for z' for the lower hemisphere is identical to the z' expression for the upper hemisphere. However, the limit for the upper border of the integration interval for r' is different: $a\sqrt{1-\frac{(z-c)^2}{c^2}}$. The expression for the lower hemisphere is obtained analogous to the upper hemisphere of the spheroid crown, i.e.

$$\frac{dI(\Omega,0,z)_{crown,\ lower}}{dz} = C\frac{2I_0\Gamma(\Omega\rightarrow-\Omega)}{G(\Omega)c}\left(e^{-2G(\Omega)u_l(z-c)}\left(\frac{z-c}{c} + \frac{1}{G(\Omega)u_l c}\right) - e^{-G(\Omega)u_l z}\left(1 + \frac{1}{G(\Omega)u_l c}\right)\right) \tag{10}$$

Eq. (9) is used when $0 \le z \le c$ and Eq. (10) is applied when $c \le z \le 2c$. Both expressions can be written as a function of LAI by substituting $\frac{3LAI}{4c}$ for u_l.

2.2. Testing the analytical expressions

In the previous section, the analytical expressions of light passing through a crown and back to the LiDAR sensor were described for cuboid, conical and spheroid crowns. To test those expressions, a set

of simplified trees with varying structural attributes is generated. These generated trees are used to create LiDAR simulations to test the analytical formulae. The modelled, detailed full 3D models allow us to control all parameters and exclude uncertainty introduced by e.g. scan angle, terrain or atmosphere.

2.2.1. Generating tree models

Three crown shapes are considered when generating simplified tree models: cuboids, cones and spheroids. Cuboid archetypes are specified by height, width and length. In this case, width and length are equal so the cross section for cuboid trees is square. Conical archetypes are determined by the height and base radius of the crown. The spheroid archetypes are parameterised by the semi-major radius and semi-minor radius and shape is obtained by rotating an ellipse around its semi-major axis. The trunk underneath the crown is constructed by a single cylinder, parameterised by its height and radius: the trunk radius is fixed at 0.2 m for every tree and the trunk height is set to a quarter of the crown height. Leaves are the only material present in the canopy (no branches etc.) and are shaped as small disks with a radius of 0.01 m. This is similar to the leaf radius of 0.025 m assumed in (North et al., 2010). Previous LiDAR studies (Koetz et al., 2007; Kotchenova et al., 2003; North et al., 2010; Sun & Ranson, 2000) used a foliage orientation function, $G(\Omega)$, of 0.5. Therefore we will use a uniform leaf angle distribution and leaves are not permitted to overlap. The final parameter used to parameterise the crown is the LAI. In this study, LAI ranges from one to six and this parameter is interpreted as the one-sided area of leaf surface per unit ground surface area (Jensen, 2007). The leaf area density function u_l is dependent on the position in the canopy. When N_v is the leaf number density (i.e. the number of leaves per unit volume) and A_l is the leaf area, the leaf area density at depth z is $u_l(z) = N_v(z)A_l$.

For the trees with an archetype crown shape, A_l is constant because all the leaves had the same dimensions and the leaf angle distribution is uniform. The leaves are spread equally over the crown and therefore N_v is constant as well. u_l is therefore constant throughout the crown and units are [m^2/m^3]. Three components are considered in the final tree models: leaves, trunk and soil. Each of these elements has its own spectral reflectance function. The functions used for these trees are similar to the reflectance properties used in previous studies (Disney et al., 2006, 2010). The birch and Sitka spruce tree models that were utilised in Disney et al. (2009) are used as realistic broadleaved deciduous and conifer tree models. The three-dimensional birch models were derived from the OnyxTREE© software (www.onyxtree.com) and were parameterised with field data obtained in a birch forest in Sweden. Radiometric properties are the same as for the archetype tree models. The 3D structure of Sitka spruce was derived from the PINOGRAM model (Leersnijder, 1992), modified as described in Disney et al. (2006).

2.2.2. LiDAR simulations

LiDAR waveforms are numerically simulated by a Monte Carlo ray tracing (MCRT) approach. In this study the *librat* MCRT model, a library of C functions, is used. This model is based on the *ararat*/*drat* MCRT model (Lewis, 1999) and has been tested in previous studies against other models (Pinty et al., 2004; Widlowski et al., 2007) as well as against observations (Disney et al., 2006, 2009, 2010). The wavelength used for the LiDAR simulations is 1064 nm and the scene reflectance is simulated as observed from nadir. The first order scattering contribution over single trees is simulated. The field-of-view (FOV), i.e. the angle which can be viewed by the sensor, is set to 0.208° for all simulations. We use a large footprint of 20 m × 20 m. We prefer a square footprint, as opposed to the more realistic circular footprint, since it makes simulations easier. The shape of the footprint has no influence on the testing because we examine whole tree waveforms and the full horizontal extent of the crown is covered by the footprint, regardless of its shape. The vertical bin step is set to 0.1 m. Sampling characteristics are defined by 100 primary sample rays per sampling unit.

2.2.3. Testing of the analytical expressions using simulated LiDAR waveforms

The analytical expressions for describing LiDAR waveform (Eqs. 5, 8–10) are tested by comparing them against the numerically MCRT simulated LiDAR waveforms. The comparison is done for both the original waveforms and their respective cumulative values. LAI parameter estimation from the waveforms is done by inversion of the analytical expressions using the Levenberg–Marquardt algorithm (Levenberg, 1944; Marquardt, 1963). The inversion is evaluated by the coefficient of variation of the root mean squared error, CV(RMSE), to determine the best fit. The CV(RMSE) is defined as the RMSE normalised to the mean of the observed reflectance values. Unlike the RMSE, CV(RMSE) is unitless. This allows CV(RMSE)s to be compared to each other easily. Furthermore the absolute prediction error (APE) is calculated. This is a measure of accuracy and is defined as $\frac{|LAI_{true}-LAI_{estimated}|}{LAI_{true}} \times 100\%$.

The analytical expressions are tested in three experiments and an overview of these experiments can be found in Table 2. The inversion strategy is tested in the first experiment. In this experiment, we use prior knowledge of the tree and crown height to subset the crown signal from the whole tree waveform correctly. The inversion approach does not require prior knowledge or assumptions about the crown shape and has no land cover constraint. Once the crown signal is extracted, we rescale the original crown extent from 0 to 100, where 0 is the top of the crown (TOC) and 100 the bottom of the crown (BOC). In reality, however, often no prior information about tree and crown height is available. Therefore we introduce a simple subset algorithm to delimit the crown signal from the whole tree waveform. We test this subset algorithm in the second experiment in which we evaluate its accuracy and precision with respect to the LAI parameter estimation. This will lead to better insight on how sensitive the analytical descriptions are when tree and crown height are not known. The aim of the subset algorithm is to find the TOC and BOC based on the comparison of the LiDAR reflectance value from a certain bin with a certain threshold. The subset algorithm searches the recorded waveform, starting at the smallest bin. The TOC is then defined as the waveform bin before the first 3 consecutive reflectance values above a certain threshold. The BOC is the first bin of the first 3 consecutive reflectance values below this threshold after the detection of the TOC. This threshold is subject to the noise in the simulated signal. Monte Carlo methods provide a stochastic simulation and will always contain (random) statistical variation, i.e. simulation noise. Disney et al. (2000) discussed that this does not have to be a disadvantage and the potential for deriving an understanding of the random error in the simulation can be considered a major advantage over numerical methods. The explicit representation of the canopy by a finite number of objects, rather than the infinitesimal (and therefore infinite number of) objects assumed in the general turbid medium approach, and hence the analytical formulae derived here, will influence the level of noise as well. The threshold we use in the subset algorithm is defined as 0.1% of the median returned reflectance and this value works for the level of noise in our simulations but remains a heuristic

Table 2
Overview of the 3 experiments that are used to test the analytical expressions.

	Testing	Tree models	Prior information about crown height
Experiment 1	Inversion strategy	Archetype crowns	Available
Experiment 2	Crown signal subset algorithm	Archetype crowns	Unavailable
Experiment 3	Crown archetype assumptions	Realistic crowns	Unavailable

value. To determine this median, zero reflectance returns are filtered out first. Alternatively, more sophisticated approaches such as Hancock et al. (2011) could be used. In the third experiment we look at how these formulae apply to more realistic 3D vegetation structures, which do not fulfil all underlying assumptions of the derived formulae and have no prior information about tree or crown height.

3. Results

The analytical expressions (Eqs. 5, 8–10) are a combination of a scaling factor and a variable part, which is dependent on z. The scaling factor is assumed to be constant for a specific archetype crown and therefore it has no influence on the shape of its LiDAR waveform. Results of the same archetypes with different macro-structure parameters show similar results. Therefore we will only discuss the results of one example per archetype for the first two experiments. Crown height for the discussed examples is 6 m; cuboid crowns have a width and length of 2 m, conical crowns have a base radius of 2 m and spheroid crowns have a semi-minor radius of 2 m.

The first experiment tests the inversion strategy that is used in this study, i.e. the accuracy of the analytical expressions for describing LiDAR scattering, tested against full 3D simulations of the same. The results of these two experiments will indicate how well the analytical expressions work when crown archetype assumptions are met.

The second experiment compares our new analytical expressions for LiDAR waveforms against the simulated waveforms for archetype trees with fixed LAI (4) with no prior information about the crown shape. Fig. 4 shows the comparison of the analytical expressions against the simulated waveforms for archetype trees with LAI 4 in the second experiment. The figure shows the optimal fit based on parameter estimation by the Levenberg–Marquardt algorithm. This figure clearly demonstrates that when the archetype crown assumptions are met, the LiDAR signal over a specific crown archetype will have a good fit with the corresponding analytical expression.

The inferred LAI values obtained by inverting the analytical expressions against the simulated waveforms of archetypes can be found in Table 3 and the evaluation statistics of the analysis are summarised in Table 4. The evaluation statistics from the first and second experiment show that the inversion of the waveform of a cuboid or spheroid crown works best when the cumulative signal is used. The average CV(RMSE) for the cumulative waveform inversion of cuboid archetypes is 0.3% when crown height is known and 0.8% with no prior knowledge of crown height. The CV(RMSE) for spheroid archetypes is 0.3%, regardless of whether or not we know the crown height. The APE of the inversion of the cumulative signal with no prior knowledge of the crown height is 7.1% for cuboid archetypes and 4.5% for spheroid archetypes. For conical crowns best fitting is achieved on the cumulative waveform (CV(RMSE) less than 0.7%), but the prediction based on the original LiDAR signal is more accurate, with an APE of 18.6% when the crown height is not known. This can also be seen in Fig. 5, which shows the MCRT simulated LiDAR waveforms of crown archetypes for LAI values ranging from one to six. This is because the cumulative LiDAR signals for different LAI values in conical crowns cover a smaller range of normalised LiDAR reflectance than the original waveforms and are therefore less distinguishable. Cumulative waveforms of cuboid and spheroid crowns are more

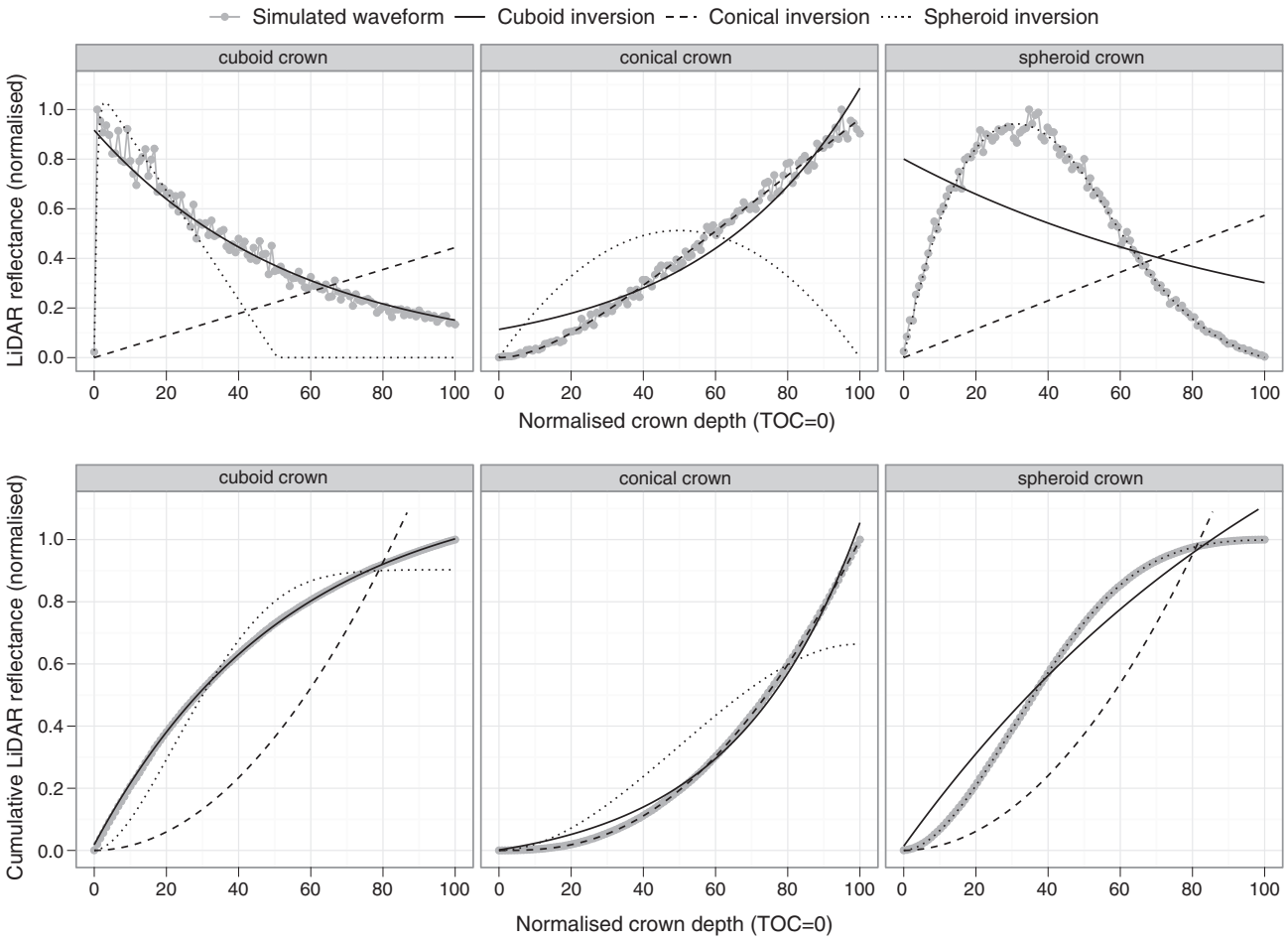

Fig. 4. Testing of the analytical expressions against simulated waveforms for archetype crowns (cuboid, conical, spheroid) with LAI 4 with no prior information of tree and crown height (experiment 2). Crown depth ranges from 0 (top of crown) to 100 (bottom of crown). (upper row) Analysis of the original waveform; (lower row) Analysis of the cumulative waveform.

Table 3
LAI estimation from the waveforms of crown archetypes based on the Levenberg–Marquardt algorithm.

	LAI estimation											
	Cuboid crown				Conical crown				Spheroid crown			
	Original		Cumulative		Original		Cumulative		Original		Cumulative	
True LAI	hA[a]	hNA[b]	hA	hNA	hA	hNA	hA	hNA	hA	hNA	hA	hNA
1	1.02	0.89	0.98	0.85	1.06	1.50	1.02	1.75	1.10	0.92	1.12	0.96
2	2.01	1.83	2.02	1.87	1.71	2.14	2.01	2.77	2.06	1.87	2.09	1.91
3	3.04	2.80	3.04	2.85	3.08	3.54	3.05	3.73	3.07	2.87	3.12	2.92
4	3.93	3.61	3.95	3.73	3.98	4.26	3.95	4.36	3.98	3.74	4.01	3.78
5	5.12	4.66	5.08	4.82	4.80	6.30	4.97	7.08	5.06	4.66	5.09	4.69
6	5.98	5.42	5.99	5.69	5.68	6.19	5.68	6.35	6.19	5.73	6.21	5.75

[a] hA = prior information about *h* (crown height) is available: experiment 1.
[b] hNA = prior information about *h* (crown height) is not available: experiment 2.

distinguishable (Fig. 5). These results from the first and second experiment show that an archetype crown can be distinguished from among the three archetypes through model fitting using the Levenberg–Marquardt algorithm.

Fig. 6 gives an overview of the testing of the analytical expressions against simulated waveforms of realistic 3D representations without prior knowledge of the crown height (experiment 3). Two birch trees and 2 Sitka spruce trees are used in this experiment, which looks at how the analytical expressions perform when the crown archetype assumptions are not met. The statistics for the inversion of the cuboid and spheroid expressions are summarised in Table 5. Fitting a cumulative spheroid waveform works best for the first birch case (Fig. 6a): CV(RMSE) is 3.1% against 8.9% for the cumulative cuboid fitting. However, the prediction of the cuboid fit (APE 25.9%) is significantly better than the prediction of the spheroid fit (APE 260.9%). The inferred LAI using the cuboid inversion is 5.4 and the inferred LAI resulting from the spheroid fit is 15.3, with the true LAI for this birch tree being 4.3. Similar findings are observed in a less extreme way in the second birch case (true LAI 4.4, Fig. 6b), where a cumulative cuboid fit with a CV(RMSE) of 3.6% has an absolute prediction error of 39.4% (inferred LAI 2.7). Cumulative spheroid fitting has a higher CV(RMSE) of 8.5%, but a better APE of 25.8% (inferred LAI 5.5). The inversion of the cumulative spheroid expression leads to the best results for both Sitka spruce case studies (Fig. 6c & d). CV(RMSE) is less than 8.1% but the absolute prediction error is high, with a minimum of 60.7%. For the first Sitka spruce tree, the inferred LAI of 3.3 is smaller than the true LAI of 8.5. The second Sitka spruce case with true LAI 15.6 has a higher APE of 78.6% with the cumulative spheroid inversion of the LiDAR signal leading to an inferred LAI of only 3.3.

4. Discussion

Our results demonstrate that the analytical expressions for first order scattering are able to reconstruct the simulated LiDAR waveforms over crown archetypes satisfactorily in most cases. The first experiment gives similar results over the whole LAI range (1 to 6). We show that the models based on crown archetypes fit the 3D simulations less well when we do not have information on tree and crown height (as will often be the case in practice). However, our results indicate that when archetype assumptions are not met, models based on these assumptions can still fit observed LiDAR signals quite well, but, crucially, only by assuming unrealistic parameter values. In particular inversion of LiDAR signals over realistic tree crowns can lead to estimates of effective LAI, which will depart from the true LAI. Given the rapidly increasing use of LiDAR in studies of canopy properties, we discuss the implications for using LiDAR models to retrieve and interpret canopy parameters.

Similar to findings in Ni-Meister et al. (2001), the key concept in these analytical expressions is the gap probability and its dependency on crown path length. The first experiment shows that the solved LAI values for crown archetypes have apparently small absolute prediction errors ranging from 1.3% to 5.5%. This shows that we established an analytical method to retrieve LAI based on the crown signal of the LiDAR waveform over crown archetypes. Not knowing tree and crown height in advance (and hence the crown signal can be delimited less accurately from the whole tree waveform) increased the absolute prediction error only marginally compared to the prediction errors from the first experiment. Results from the second experiment show that the prediction error increases by 5.8% for cuboid crowns, 13.1% for conical crowns and 0.1% for spheroid crowns. These marginal increases in prediction errors suggest that when the inversion method is applied with no prior knowledge of the crown extent or shape, it will still give an accurate estimate of the true LAI.

The results from the third experiment illustrate the importance of accurate crown signal detection within the whole tree waveform and the effect of within-crown clumping. The second Sitka spruce case (Fig. 6d) illustrates the importance of accurate crown signal detection. The simple subset algorithm we introduced fails to distinguish between crown and the lower branches because it requires the returned LiDAR reflectance to fall below a set threshold to detect the BOC. The signal from the lower branches will fuse with the crown signal and will indicate a wrong BOC. This will lead to a biased input signal for the inversion algorithm and therefore optimal inversion is not achieved. In the archetype trees, crowns were well defined and no lower branching was present. Therefore the simple subset algorithm to detect the crown signal in the whole tree waveform worked well in those cases. The results with the real trees suggest

Table 4
Evaluation statistics of experiment 1 and 2: coefficient of variation of the RMSE and absolute prediction error averaged over LAI values one to six for crowns archetypes.

	Cuboid crown				Conical crown				Spheroid crown			
	Original		Cumulative		Original		Cumulative		Original		Cumulative	
	hA[a]	hNA[b]	hA	hNA	hA	hNA	hA	hNA	hA	hNA	hA	hNA
CV(RMSE) [%]	8.8	21.2	0.3	0.8	6.0	6.0	0.4	0.7	5.3	5.4	0.3	0.3
APE [%]	1.5	8.7	1.3	7.1	5.5	18.6	1.9	32.4	3.3	6.0	4.4	4.5

[a] hA = prior information about *h* (crown height) is available: experiment 1.
[b] hNA = prior information about *h* (crown height) is not available: experiment 2.

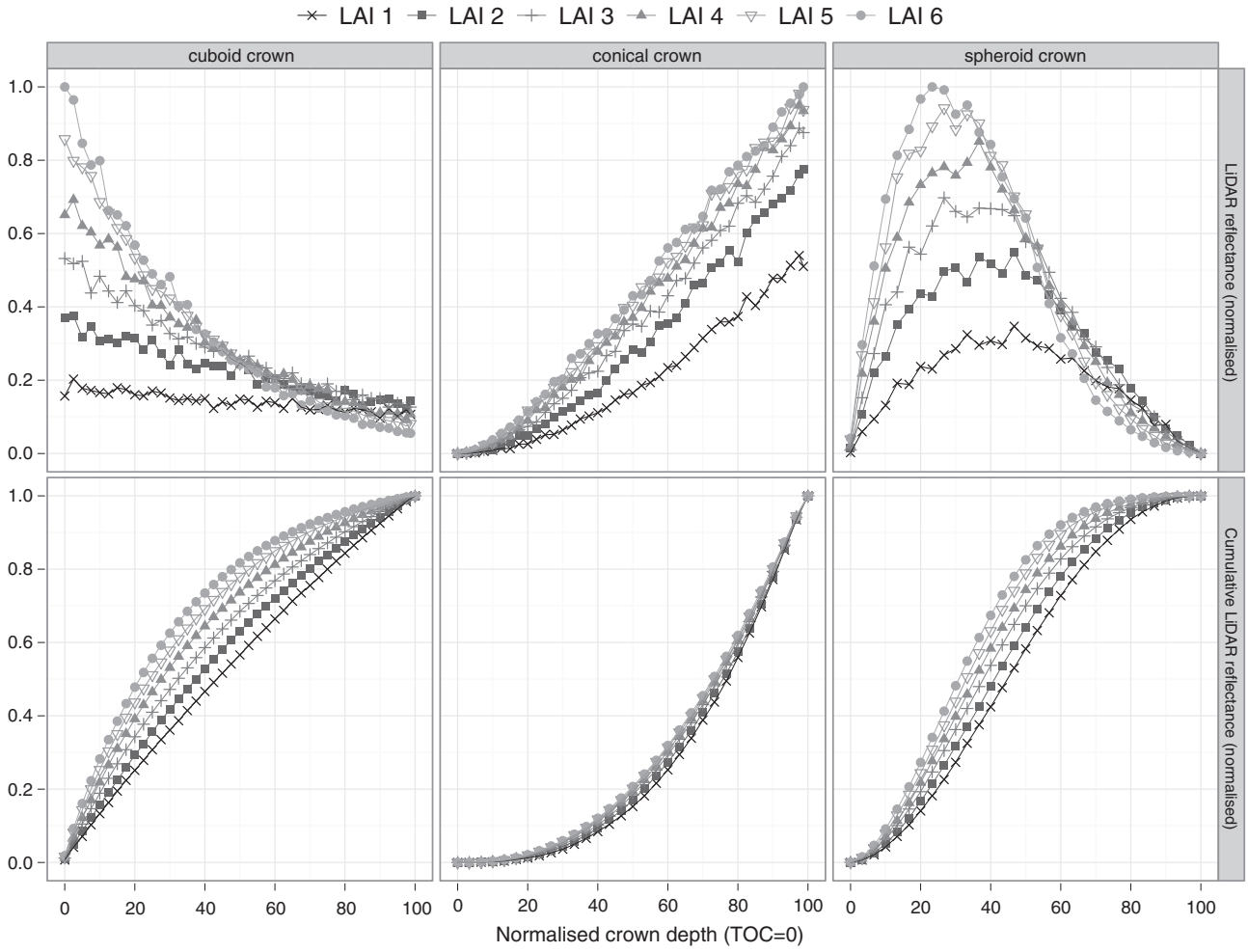

Fig. 5. MCRT simulated LiDAR waveforms of crown archetypes (cuboid, conical, spheroid) for different LAI values. (upper row) Original waveform; (lower row) Cumulative waveform.

the need for a more robust method to delimit the correct crown signal in more realistic circumstances. Also the effect of topography plays an important role in the correct delineation of the crown signal from a large footprint LiDAR waveform. If the tree is located on a sloping terrain, the vegetation and ground return might overlap in the LiDAR waveform (Hancock et al., 2012). Approaches to reduce the effect of slope on the LiDAR signal could use a sensor design that is susceptible to the differences in the traits of vegetation and ground, such as multi-wavelength instruments. Alternatively, a digital terrain model could be used to predict the influence of the ground signal on the LiDAR signal.

The analytical expressions describe the LiDAR signal of a single tree having the full horizontal extent of the crown covered by the footprint. The shape of the LiDAR signal over multiple trees might become less distinct. For non-overlapping crowns, the resulting waveform would be the summation of linear transformations of the individual crown waveforms, which are quantified by the analytical expressions for single crowns. We cannot deal with partial crowns (other than the cuboid archetype) so the results are only directly applicable to waveforms that contain some integer number of trees. A common approach to overcome this issue is by re-sampling smaller footprint LiDAR to mimic large footprint waveforms over single trees. Blair and Hofton (1999) aggregated high resolution small footprint elevation to mimic the footprint waveform of the LVIS instrument. Popescu et al. (2011) and Muss et al. (2011) both used discrete return LiDAR to create pseudo-waveforms. Popescu et al. (2011) used simulated pseudo-waveforms from airborne LiDAR to compare retrieval of aboveground biomass and forest structure between GLAS and airborne LiDAR. Muss et al. (2011) aggregated discrete LiDAR height and intensity into larger footprints so they could use the characteristics of traditional waveform LiDAR to asses forest structure. Reitberger et al. (2008) used small footprint waveform LiDAR in combination with tree segmentation to derive forest characteristics at tree level. Such an approach would depend on the forest type and how reliable trees could be isolated. Trees could be isolated more easily in open forest types (e.g. savanna), but it will be more challenging to isolate trees in denser environments (e.g. rainforest). Tang et al. (2012) derived LAI in tropical rainforests from LVIS waveforms (25 m footprint) with moderate success (R^2 ranging from 0.42 to 0.63) using the light transmittance within the canopy. The LVIS footprint covered multiple trees and the formulae used in their work implicitly assumed a crown shape equating to the cuboid crown archetype. If we take their analysis as typical, then the assumptions we tested in our abstraction are no different from those used in practice.

The plots in Fig. 6 illustrate that when the inversion method is applied to realistic tree crowns, which do not follow one of the assumed archetypes quite closely, the analytical expressions do not work so well. This may perhaps appear unsurprising: where the model assumptions are not met, our simplified models fail to pick up key aspects of the LiDAR signal. However many of the current approaches to modelling LiDAR signals in airborne laser scanning applications use some sort of assumption of crown archetype (Table 1), and these models of course allow retrieval of parameters such as LAI

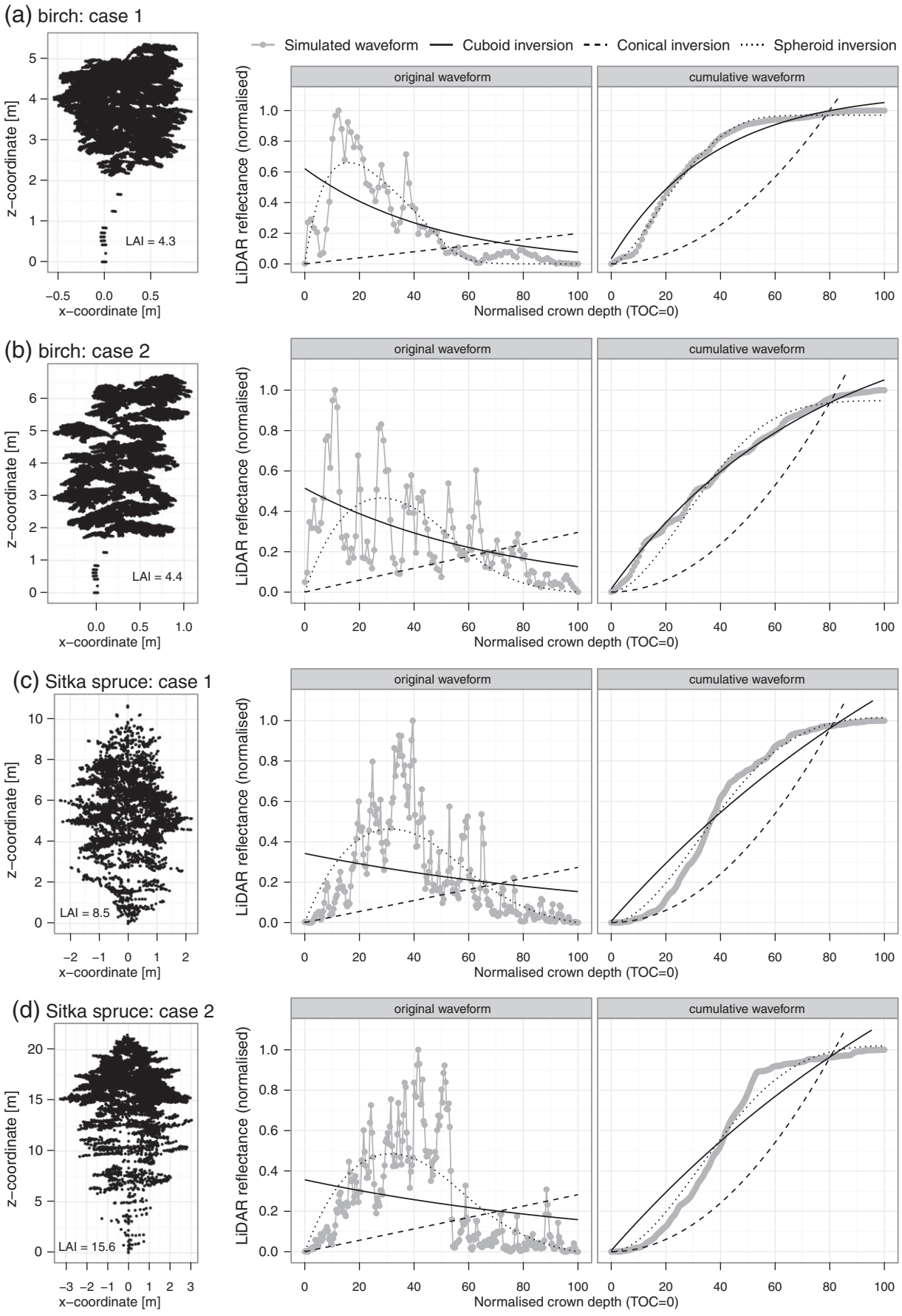

Fig. 6. Testing of the analytical expressions against simulated waveforms for realistic 3D tree representations (experiment 3). (left) xz-cross-section of the tree structure; (middle) Analysis of the original waveform; (right) Analysis of the cumulative waveform.

Table 5
Estimated LAI values and evaluation statistics for realistic 3D trees (experiment 3).

			Birch: case 1	Birch: case 2	Sitka spruce: case 1	Sitka spruce: case 2
		True LAI	4.3	4.4	8.5	15.6
Cuboid	Original	Estimated LAI	4.2	2.8	1.6	1.6
		CV(RMSE) [%]	86.1	68.1	99.0	102.6
		APE [%]	1.2	36.1	81.2	89.6
	Cumulative	Estimated LAI	5.4	2.7	1.3	1.3
		CV(RMSE) [%]	8.9	3.6	16.6	17.9
		APE [%]	25.9	39.4	84.9	91.7
Spheroid	Original	Estimated LAI	16.3	5.1	3.7	3.7
		CV(RMSE) [%]	52.8	75.2	66.4	69.6
		APE [%]	284.2	14.9	56.6	76.5
	Cumulative	Estimated LAI	15.3	5.5	3.3	3.3
		CV(RMSE) [%]	3.1	8.5	6.8	8.1
		APE [%]	260.9	25.8	60.7	78.6

and crown height. Our results show that caution should be given to the impact of such assumption on inferring biophysical parameters. Fig. 6 suggests that, although assuming a crown archetype will provide a result, it can potentially be misleading when measured crowns depart from the archetypes. Similar conclusions were drawn in Calders et al. (2012), where LAI was inferred from realistic trees with lower LAI values (LAI ranging from 0.3 to 3.1 for eucalyptus and from 0.3 to 2.2 for birch).

The second birch case (Fig. 6b) is a good example of the effect of clumping on the waveform. This effect is clearly visible in the original LiDAR waveform. The cumulative waveform is more robust and hence less affected by clumping. Severe clumping means that the assumption of constant leaf area density is severely violated, so it is not surprising that results are poor (Table 5). This is especially true in both birch cases, where the best fitting archetype does not necessarily lead to the most realistic inverted LAI value. The results from the birch cases also illustrate the advantage of an inversion method which does not make any prior assumptions about crown archetype according to tree species as opposed to many current LiDAR studies. A spheroid crown fits best for the first birch case, but a cuboid crown provides a better fit for the second birch case. It is important to stress that, as mentioned above, best fit does not equate to best LAI inversion for the birch cases. In Kotchenova et al. (2003) a time-dependent stochastic radiative transfer theory was introduced to model the propagation of laser pulses in the crown and this was solved numerically. The approach allowed for a more realistic description of the canopy structure including clumping and gaps. A factor was used to describe the correlation between foliage elements in different layers (vertical heterogeneity). Although additional improvements need to be made to provide more accurate characterisation of the probability density function, this probability-based approach has the potential to improve our approach.

This work demonstrates the implications of crown archetype assumptions on inferring biophysical parameters from LiDAR signals. Canopy parameters inferred from realistic canopies using the archetype assumptions can be misleading as they are essentially effective parameters. That is, these derived parameters may be consistent with the assumptions of archetypes and hence allow inversion against observations, but they will not correspond to physically-measurable versions of these parameters. The key for applications of such models is understanding how the effective parameters are related to the real ones. We suggest that an analysis of the departure of the true waveform from the inverted waveform will provide more knowledge about the vertical clumping of all crown constituents. Clumping, along with the slope issue, is an area for future work. The analytical expressions, together with a MCRT radiative transfer to model LiDAR signals, are an ideal approach to further explore these issues.

5. Conclusions

Our research demonstrates a method for exploring the assumptions of crown archetypes, typically made when modelling LiDAR signals for parameter estimation. A unique feature of this work is the development of a new set of analytical expressions to describe LiDAR waveforms. Analytical expressions for three archetype crowns are derived based on the radiative transfer solution for single order scattering in the optical case. These expressions are tested against MCRT waveform simulations using a curve-fitting optimisation approach. Using simulations enabled us to control all aspects of the crown architecture and sensor properties to test the implications of such crown archetype assumptions for inferring LAI from LiDAR waveforms. Overall agreement is shown between the expressions and simulated signals over simplified trees. LAI estimates demonstrate only a small prediction error, even when there is no prior knowledge of the crown height for such trees. We then demonstrated that the analytical expressions did not function well when applied to more realistic 3D representations of broadleaved deciduous (LAI ranging from 4.3 to 4.4) and evergreen needle-leaved (LAI ranging from 8.5 to 15.6) crowns, which depart significantly from the crown archetypes. Even if an archetype waveform fits the realistic data, it can potentially have very large (up to 260.9%, typically ranging from 39.4% to 78.6%) errors in inferred LAI. We suggest this discrepancy is largely due to within-crown clumping of the crown constituents. Our results indicate that assuming crown archetypes for parameter retrieval from LiDAR may be problematic if within-crown clumping is not accounted for. Such a negative outcome is of importance as LAI is closely related to forest structure and plays an important role in forest ecosystems. The increasing use of LiDAR for forestry suggest prudence is needed in inferring LAI based on crown archetypes. These inferred values are essentially effective parameters that will not be measurable in practice.

Acknowledgements

The authors thank the anonymous reviewers for their valuable suggestions to improve the manuscript. We also thank R. Dubayah for his helpful comments on the manuscript.

Appendix A

Nomenclature

$\Gamma(\Omega_0 \rightarrow \Omega_s)$	Area scattering phase function
κ_e	Optical extinction coefficient
Ω_0	Direction of incident LiDAR pulse
Ω_s	Direction of scattering
C	Canopy cover
H	Tree height [m]
h	Crown height [m]

R	Base radius of conical crown [m]
r'	An intermediate position along the radius axis
u_l	Leaf area density function [m^2/m^3]
z	Penetration depth with top of the crown as reference (TOC = 0)
z'	Effective crown penetration
A_l	Leaf area [m^2]
a	Semi-minor radius of prolate spheroid crown [m]
c	Semi-major radius of prolate spheroid crown [m]
$I(\Omega_s, z)$	Received backscatter by the sensor
I	Intensity (radiance or brightness) [W m^{-2} sr^{-1}]
N_v	Leaf number density [leaves/m^2]
$P(\Omega_0 \rightarrow \Omega_s)$	Volume scattering phase function

References

Barbier, N., Proisy, C., Véga, C., Sabatier, D., & Couteron, P. (2011). Bidirectional texture function of high resolution optical images of tropical forest: An approach using LiDAR hillshade simulations. *Remote Sensing of Environment*, *115*, 167–179.

Blair, J. B., & Hofton, M. A. (1999). Modeling laser altimeter return waveforms over complex vegetation using high-resolution elevation data. *Geophysical Research Letters*, *26*, 2509–2512.

Calders, K., Lewis, P., Disney, M., Verbesselt, J., Armston, J., & Herold, M. (2012). Effects of clumping on modelling LiDAR waveforms in forest canopies. *IEEE International Geoscience and Remote Sensing Symposium (IGARSS)* (pp. 3391–3394).

Disney, M. I., Kalogirou, V., Lewis, P., Prieto-Blanco, A., Hancock, S., & Pfeifer, M. (2010). Simulating the impact of discrete-return lidar system and survey characteristics over young conifer and broadleaf forests. *Remote Sensing of Environment*, *114*, 1546–1560.

Disney, M. I., Lewis, P., Bouvet, M., Prieto—Blanco, A., & Hancock, S. (2009). Quantifying surface reflectivity for spaceborne lidar via two independent methods. *IEEE Transactions on Geoscience and Remote Sensing*, *47*, 3262–3271.

Disney, M. I., Lewis, P., & North, P. R. J. (2000). Monte Carlo ray tracing in optical canopy reflectance modelling. *Remote Sensing Reviews*, *18*, 163–196.

Disney, M., Lewis, P., & Saich, P. (2006). 3D modelling of forest canopy structure for remote sensing simulations in the optical and microwave domains. *Remote Sensing of Environment*, *100*, 114–132.

Ferraz, A., Bretar, F., Jacquemoud, S., Gonçalves, G., Pereira, L., Tomé, M., et al. (2012). 3-D mapping of a multi-layered mediterranean forest using ALS data. *Remote Sensing of Environment*, *121*, 210–223.

Goodwin, N. R., Coops, N. C., & Culvenor, D. S. (2007). Development of a simulation model to predict LiDAR interception in forested environments. *Remote Sensing of Environment*, *111*, 481–492.

Hancock, S., Disney, M., Muller, J. -P., Lewis, P., & Foster, M. (2011). A threshold insensitive method for locating the forest canopy top with waveform lidar. *Remote Sensing of Environment*, *115*, 3286–3297.

Hancock, S., Lewis, P., Foster, M., Disney, M., & Muller, J. -P. (2012). Measuring forests with dual wavelength lidar: A simulation study over topography. *Agricultural and Forest Meteorology*, *161*, 123–133.

Hyde, P., Dubayah, R., Peterson, B., Blair, J. B., Hofton, M., Hunsaker, C., et al. (2005). Mapping forest structure for wildlife habitat analysis using waveform lidar: Validation of montane ecosystems. *Remote Sensing of Environment*, *96*, 427–437.

Jensen, J. R. (2007). *Remote Sensing of the Environment: An Earth Resource Perspective* (2nd ed.). : Prentice Hall (608 pp.).

Kato, A., Moskal, L. M., Schiess, P., Swanson, M. E., Calhoun, D., & Stuetzle, W. (2009). Capturing tree crown formation through implicit surface reconstruction using airborne lidar data. *Remote Sensing of Environment*, *113*, 1148–1162.

Koch, B., Heyder, U., & Weinacker, H. (2006). Detection of individual tree crowns in airborne lidar data. *Photogrammetric Engineering and Remote Sensing*, *72*, 357–363.

Koetz, B., Sun, G., Morsdorf, F., Ranson, K. J., Kneubühler, M., Itten, K., et al. (2007). Fusion of imaging spectrometer and LIDAR data over combined radiative transfer models for forest canopy characterization. *Remote Sensing of Environment*, *106*, 449–459.

Kotchenova, S. Y., Shabanov, N. V., Knyazikhin, Y., Davis, A. B., Dubayah, R., & Myneni, R. B. (2003). Modeling lidar waveforms with time-dependent stochastic radiative transfer theory for remote estimations of forest structure. *Journal of Geophysical Research*, *108*(D15), 4484.

Leersnijder, R. P. (1992). Pinogram: A pine growth area model. *Ecological Modelling*, *61*, 1–147.

Lefsky, M. A., Cohen, W. B., Acker, S. A., Parker, G. G., Spies, T. A., & Harding, D. (1999). Lidar remote sensing of the canopy structure and biophysical properties of Douglas-fir western hemlock forests. *Remote Sensing of Environment*, *70*, 339–361.

Levenberg, K. (1944). A method for the solution of certain non—linear problems in least squares. *Quarterly of Applied Mathematics*, *2*, 164–168.

Lewis, P. (1999). Three-dimensional plant modelling for remote sensing simulation studies using the Botanical Plant Modelling System. *Agronomie, Agriculture and Environment*, *19*, 185–210.

Lim, K., Treitz, P., Baldwin, K., Morrison, I., & Green, J. (2003). Lidar remote sensing of biophysical properties of tolerant northern hardwood forests. *Canadian Journal of Remote Sensing*, *29*, 658–678.

Marquardt, D. W. (1963). An algorithm for least-squares estimation of nonlinear parameters. *Journal of the Society for Industrial and Applied Mathematics*, *11*, 431–441.

Muss, J. D., Mladenoff, D. J., & Townsend, P. A. (2011). A pseudo-waveform technique to assess forest structure using discrete lidar data. *Remote Sensing of Environment*, *115*, 824–835.

Nelson, R. (1997). Modeling forest canopy heights: The effect of canopy shape. *Remote Sensing of Environment*, *60*, 327–334.

Ni-Meister, W., Jupp, D. L. B., & Dubayah, R. (2001). Modeling lidar waveforms in heterogeneous and discrete canopies. *IEEE Transactions on Geoscience and Remote Sensing*, *39*, 1943–1958.

North, P. R. J., Rosette, J. A. B., Suárez, J. C., & Los, S. O. (2010). A Monte Carlo radiative transfer model of satellite waveform LiDAR. *International Journal of Remote Sensing*, *31*, 1343–1358.

Pinty, B., Widlowski, J. -L., Taberner, M., Gobron, N., Verstraete, M. M., Disney, M., et al. (2004). Radiation transfer model intercomparison (RAMI) exercise: Results from the second phase. *Journal of Geophysical Research*, *109*, D06210.

Popescu, S. C., Zhao, K., Neuenschwander, A., & Lin, C. (2011). Satellite lidar vs. small footprint airborne lidar: Comparing the accuracy of aboveground biomass estimates and forest structure metrics at footprint level. *Remote Sensing of Environment*, *115*, 2786–2797.

Reitberger, J., Krzystek, P., & Stilla, U. (2008). Analysis of full waveform LIDAR data for the classification of deciduous and coniferous trees. *International Journal of Remote Sensing*, *29*, 1407–1431.

Riaño, D., Chuvieco, E., Condés, S., González-Matesanz, J., & Ustin, S. L. (2004). Generation of crown bulk density for *Pinus sylvestris* L. from lidar. *Remote Sensing of Environment*, *92*, 345–352.

Ross, J. (1981). *The radiation regime and architecture of plant stands*. The Hague: W. Junk Publishers (391 pp.).

Sun, G., & Ranson, K. J. (2000). Modeling lidar returns from forest canopies. *IEEE Transactions on Geoscience and Remote Sensing*, *38*, 2617–2626.

Tang, H., Dubayah, R., Swatantran, A., Hofton, M., Sheldon, S., Clark, D. B., et al. (2012). Retrieval of vertical lai profiles over tropical rain forests using waveform lidar at La Selva, Costa Rica. *Remote Sensing of Environment*, *124*, 242–250.

Vauhkonen, J., Tokola, T., Maltamo, M., & Packalén, P. (2009). Applied 3D texture features in ALS-based forest inventory. *European Journal of Forest Research*, *129*, 803–811.

Wang, C., & Glenn, N. F. (2008). A linear regression method for tree canopy height estimation using airborne lidar data. *Canadian Journal of Remote Sensing*, *34*, S217–S227.

Widlowski, J. -L., Taberner, M., Pinty, B., Bruniquel-Pinel, D., Disney, M., Fernandes, R., et al. (2007). Third radiation transfer model intercomparison (RAMI) exercise: Documenting progress in canopy reflectance models. *Journal of Geophysical Research*, *112*, D09111.